Effective Steady-State Recombination Decay Times in Comparison to Time-Resolved Photoluminescence Decay Times in Halide Perovskite Solar Cells

Chris Dreessen,* Lidón Gil-Escrig, Markus Hülsbeck, Michele Sessolo, Henk J. Bolink, and Thomas Kirchartz*

One of the key topics in perovskite solar cells is the reduction of charge carrier recombination, with the aim of increasing power conversion efficiency. The recombination lifetime is a commonly used tool, as it directly affects the current–voltage curve via the diffusion length. The lifetime is often estimated using time-domain measurement methods such as time-resolved photoluminescence. However, two obstacles emerge when applying the transiently measured decay times to the steady-state theory. In general, the decay time depends on the charge carrier concentration, and it is often not clear under which conditions the transient measurement must be conducted to be comparable with the steady-state performance of the device. Furthermore, diffusion and capacitive effects due to charge injection and extraction can influence transient techniques and cause the measured decay time to deviate from the sought-after recombination lifetime. Voltage-dependent steady-state photoluminescence measurements can be used to estimate the internal voltage during device operation and allow the extraction of collection efficiencies and effective steady-state decay times that are independent of transport and capacitive effects. Here, the differences between the steady-state and transient decay times are identified and discussed, and the losses in the current–voltage curve caused by extraction issues are quantified.

1. Introduction

Solar cells employing lead-halide perovskites have reached in a short time span of 10 years striking power conversion efficiencies (PCEs) of 26.7% in single-junction devices.[1] In addition, the mixing of halides enables to tune the bandgap of perovskites optimally for tandem devices, together with silicon even higher PCEs of 34.6% were achieved.[1–3] Along with the high absorption coefficients, the low exciton binding energies, and the high photoluminescence quantum yields, one reason for the success of perovskites is the long charge carrier lifetime that reflects low recombination losses and permits long diffusion lengths for good charge transport.[4–9] Recently, it was shown that the low mobilities of the often-organic charge transport layers (CTLs) may be responsible for potential transport losses, but also these issues are minimized by long recombination lifetimes.[10,11] However, while it is commonly understood that long decay times are good for device perfor-

mance, a framework to put the experimental results in context is often missing. Stating only a single number for the decay time without further information about the measurement conditions is a dangerous habit because the recombination lifetime is generally dependent on the charge carrier concentration in the perovskite.[12,13] This is true for all semiconductors once the photogenerated carrier density exceeds the doping density but it is of particular relevance for lead-halide perovskites as they have extremely low intrinsic doping densities.[14] The consequence that the lifetime can change under different excitation or extraction conditions is important for classifying the measured values in terms of the steady-state performance of the current–voltage curve.[15] Lifetimes at arbitrary conditions are not necessarily the lifetimes that control the device efficiency. Moreover, there are many ways to determine a decay time experimentally, such as time-resolved photoluminescence (TRPL),[12,16] transient photovoltage/open-circuit voltage decay,[16,17] transient absorption spectroscopy,[18] time-delayed collection field,[19] and small perturbation methods in the frequency domain.[19] However, it is questionable whether the decay times obtained by these experimental methods actually reflect the recombination lifetimes in the

C. Dreessen, M. Hülsbeck, T. Kirchartz
IMD-3 – Photovoltaics
Forschungszentrum Jülich
52425 Jülich, Germany
E-mail: c.dreessen@fz-juelich.de; t.kirchartz@fz-juelich.de

L. Gil-Escrig, M. Sessolo, H. J. Bolink
Instituto de Ciencia Molecular, ICMol
Universidad de Valencia
C/Catedrático J. Beltrán 2, 46980 Paterna, Spain

T. Kirchartz
Faculty of Engineering and CENIDE
University of Duisburg-Essen
Carl-Benz-Str. 199, 47057 Duisburg, Germany

perovskite. The deviation between theory and experiment often originates from different definitions of the same parameter. Recently, decay times of several hundred μs were shown, exceeding the expected value according to the photoluminescence quantum yield of the films which is indicative of a discrepancy between the decay time in transient experiments and the steady-state recombination rate.[20] Thus, the experimental measurements leave two questions that are hidden in many reports about the lifetime: 1) under which conditions should the transient measurement be conducted to compare it to the steady-state operation and 2) do the measured decay times correspond to the actual recombination lifetimes that describe the steady-state performance?

Here, we address these questions by comparing TRPL decay times with effective decay times obtained via voltage-dependent steady-state photoluminescence measurements, where we explicitly consider the finite efficiency of extraction that leads to high light-induced carrier concentrations at short circuit and maximum power point inside the absorber layer. We quantify extraction losses at any operating point using the example of coevaporated wide-bandgap perovskite solar cells.

2. Device Characteristics

In this study, the extraction characteristics and recombination lifetimes of p–i–n solar cells with varying thicknesses of the hole extraction layer (HTL) consisting of poly[bis(4-phenyl)(2,4,6-trimethylphenyl)amine (PTAA) were investigated. The absorber layer is a coevaporated methylammonium lead iodide bromide MAPb(I$_{0.85}$Br$_{0.15}$)$_3$ perovskite with a bandgap of 1.68 eV which was introduced recently as a wide-bandgap absorber for tandem applications with silicon (absorbance and X-ray diffraction [XRD] shown in Figure S1, Supporting Information).[21] The complete device stack is depicted in the inset of **Figure 1**a. The different PTAA thicknesses lead to several effects on the current–voltage (J–V) curves (Figure 1a), as indicated by the J–V parameters (Figure 1b–e). The PTAA thickness is affected by changing the concentration of the polymer in the solution used to spin coat the film. Hence, rather than obtaining the PTAA thickness we refer to the PTAA concentration in the spin coating solution. The device with the lowest PTAA concentration (PTAA 1.5 mg mL^{-1}) has the highest PCE of 17%, mainly due to the higher short-circuit current density J_{sc}, while the open-circuit voltage V_{oc} is lower than that of the samples made with the other two concentrations (PTAA 3 mg mL^{-1} and PTAA 6 mg mL^{-1}). For the thickest HTL layer (PTAA 6 mg mL^{-1}), the fill factor FF decreases. Therefore, the set of devices shows different behaviors for each PTAA concentration, making it a good showcase for different extraction properties.

3. Charge Carrier Concentrations in the Perovskite under Steady-State Operating Conditions of the Solar Cell

The aim of this manuscript is to show which recombination lifetimes are relevant during the operating conditions of solar cells. But first we want to give a short summary explaining the basics of recombination and charge carrier lifetimes in halide perovskites. The effective recombination lifetime τ_{eff} for electrons (holes) is
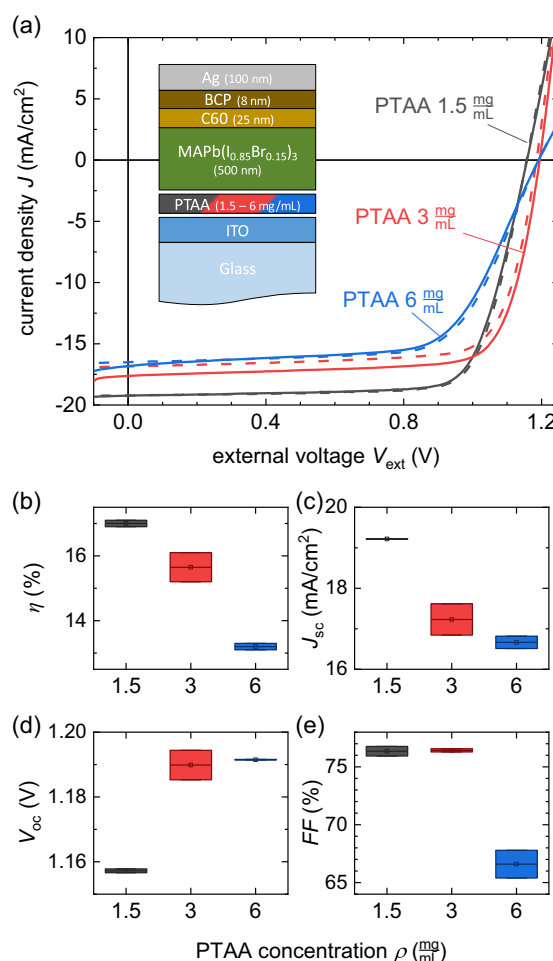
Figure 1. Device characteristics. a) J–V curves of devices with three different PTAA thicknesses. The solid (dashed) lines show the forward (reverse) direction. The inset shows the complete p–i–n device stack of the solar cells, thicknesses not to scale. b) PCE η, c) short-circuit current density J_{sc}, d) open-circuit voltage V_{oc}, and e) the FF as a function of the PTAA concentration ρ.

traditionally thought of as the characteristic time constant of an exponential decay of the average electron (hole) density after a pulsed excitation. This is fulfilled for the historically typical case of a doped semiconductor in low-level injection. In different cases, however, the carrier density does not precisely decay exponentially, so that several somewhat different definitions for effective lifetimes in transients have been developed and used. Next to monoexponential fits, bi- and stretched exponentials have been used to extract an average or several decay times.[6,8,22,23] Since the lifetime is generally dependent on the charge carrier concentration, we recommend using the differential approach.[24,25] Furthermore and fundamentally different, a lifetime can also be defined under steady-state excitation as the ratio of the excess electron concentration Δn (assumed to equal the excess hole concentration Δp) and the total recombination rate R at this charge carrier concentration is[26]

$$\tau_{eff} = \frac{\Delta n}{R(n,p)} = \frac{\Delta n}{R_{SRH}(n,p) + R_{rad}(n,p) + R_{Auger}(n,p)}. \quad (1)$$

Here, R_{SRH}, R_{rad}, and R_{Auger} are the Shockley–Read–Hall, radiative, and Auger recombination rates, respectively, which all depend on n and p. Perovskites typically have such a low doping concentration that they behave like an intrinsic semiconductor for which no simplification of the recombination rates can be applied.[14,27,28] However, the low doping density also ensures that under typical experimental injection conditions the equilibrium carrier concentrations are negligible and $\Delta n \approx n$ holds.

The dependence of the radiative and Auger recombination rates on the charge carrier concentration is[12]

$$R_{rad}(n) = [k_{rad}(1 - p_r)](np - n_i^2) \propto n^2, \tag{2}$$

$$R_{Auger}(n) = C_n(n^2 p - n_0^2 p_0) + C_p(p^2 n - p_0^2 n_0) \propto n^3, \tag{3}$$

where on the right-hand side $n = p$ was assumed for simplicity to show the proportionality. The parameters k_{rad}, p_r, C_n, and C_p are the radiative recombination coefficient, the reabsorption probability, and the electron and hole Auger coefficients, respectively. The intrinsic charge carrier concentration $n_i = \sqrt{N_C N_V} \exp[-(E_C - E_V)/2kT]$ depends on the effective density of states N_C and N_V and the energy levels E_C and E_V of the conduction and valence band, respectively. If any of these two types of recombination are significant, the recombination lifetime will decrease with the charge carrier concentration. For trap-mediated recombination, the dependence on n changes with the relation of the electron and hole quasi-Fermi levels to the energy level E_T of the trap as this affects the detrapping rates back into the bands. In the Shockley–Read–Hall formalism,[26] this is expressed by the parameters $n_1 = N_C \exp[-(E_C - E_T)/(kT)]$ and $p_1 = N_V \exp[-(E_T - E_V)/(kT)]$ that correspond to the electron and hole densities when the corresponding quasi-Fermi level matches the trap energy level, respectively. It is important to note that n_1 and p_1 do not refer to actual charge carrier concentrations that exist in the semiconductor but rather serve as thresholds for when a trap is considered shallow and when deep. For example, for shallow traps with energies close to the valence band and above the electron quasi-Fermi level, detrapping of electrons is more likely to happen ($n_1 \gg n$) than for deep traps ($n_1 \ll n$), which reduces the recombination rate. Under these circumstances, the trap occupation is close to zero but increases linearly with the charge carrier density. On the contrary, a deep trap at midgap has the largest energy difference from both bands and is therefore least affected by detrapping. In this situation (when the trap level is between the quasi-Fermi levels), the trap occupation is independent of the charge carrier concentration and depends solely on the capture coefficients. Mathematically, the trap-mediated recombination of an intrinsic semiconductor at steady-state conditions is formulated by[12,26]

$$R_{SRH}(n) = \frac{(np - n_i^2)}{(n + n_1)\tau_{SRH,p} + (p + p_1)\tau_{SRH,n}}$$

$$\propto \begin{cases} n & \text{for } n \gg n_1, p_1 \\ n^2 & \text{for } n_1 \text{ or } p_1 \gg n \\ n^\delta, \quad 1 < \delta < 2, & \text{for } n \approx n_1 \text{ or } p_1 \end{cases} \tag{4}$$

Here, $\tau_{SRH,n}$ and $\tau_{SRH,p}$ are the SRH electron and hole lifetimes. It is important to point out that $\tau_{SRH,n}$ and $\tau_{SRH,p}$ are

constants that depend only on the capture coefficient and the density of trap states.[29] Hence, they are parameters describing the trap while τ_{eff} rather refers to the charge carriers and changes with charge carrier concentration.

Therefore, it is important to quantify the carrier concentration inside the perovskite layer during the steady-state operation of the solar cell under AM1.5G illumination to be able to make sense of decay time data obtained from measurements such as TRPL. Per definition, in steady state, the rate of charge carriers generated in the device is the same as the rate of charge carriers leaving the device, either by electrical extraction or by recombination. As the excitation of electrons and holes leads to a shift of their quasi-Fermi levels $E_{F,n}$ and $E_{F,p}$ (see **Figure 2**a) closer to the conduction and valence band, respectively, a constant quasi-Fermi-level splitting ΔE_F is established which is also sometimes referred to as an internal voltage V_{int}. In an intrinsic semiconductor, the relation between Fermi-level splitting, internal voltage, and carrier density is given by

$$\Delta E_F = qV_{int} = kT \ln\left(\frac{np}{n_i^2}\right), \tag{5}$$

where q is the elementary charge, k the Boltzmann constant, and T the temperature of the carriers in the perovskite. However, it is important to notice that even in equilibrium these quantities are not necessarily independent of the position throughout the device. The external voltage V_{ext}, electrically measured or applied at the electrodes, can be significantly different from the V_{int} inside the absorber layer, especially in the presence of a current flow.

One way to obtain V_{int} is via the photoluminescence (PL) arising from radiative recombination in the absorber layer. Hence, the PL is a measure of the average ΔE_F, or qV_{int}, inside the perovskite bulk. By voltage-dependent PL measurements in full devices, it was shown for a variety of halide perovskites and other solar cell technologies that V_{int} and V_{ext} are deviating strongly; only at open circuit they usually coincide if no large energy offset between the conduction/valence bands of the perovskite and electron/hole transport layer (ETL/HTL) exists.[11,30–36] As an example, Figure 2b shows the PL spectra of the PTAA 3 mg mL^{-1} device as a function of the externally applied voltage while illuminated with laser radiation at 532 nm with the power density that generates charge carriers equivalent to the AM1.5G sun spectrum (61.5 mW cm^{-2}). The corresponding figures for the other devices can be found in Figure S2, Supporting Information. At high external voltages above 0.9 V, the intensity of the spectra increases clearly, while at low voltages the spectra are almost identical. We note that special care was taken to exclude collecting luminescence from regions of the sample outside the contacted area and that this phenomenon is not given by spots of high series resistance, but the luminescence is homogeneously emitted from the contacted area.[11] From the PL spectra, one can estimate the internal voltage via several methods.[9] Here, we employ a method that uses the integration of the PL spectra. Integrating the spectra results in a photon flux ϕ which is proportional to the product of the charge carrier concentrations, so that according to Equation (5), it follows $qV_{int} = kT \ln(\phi c_{cal}^{-1})$, with the constant calibration factor c_{cal}. This calibration factor is influenced by the calibration of the
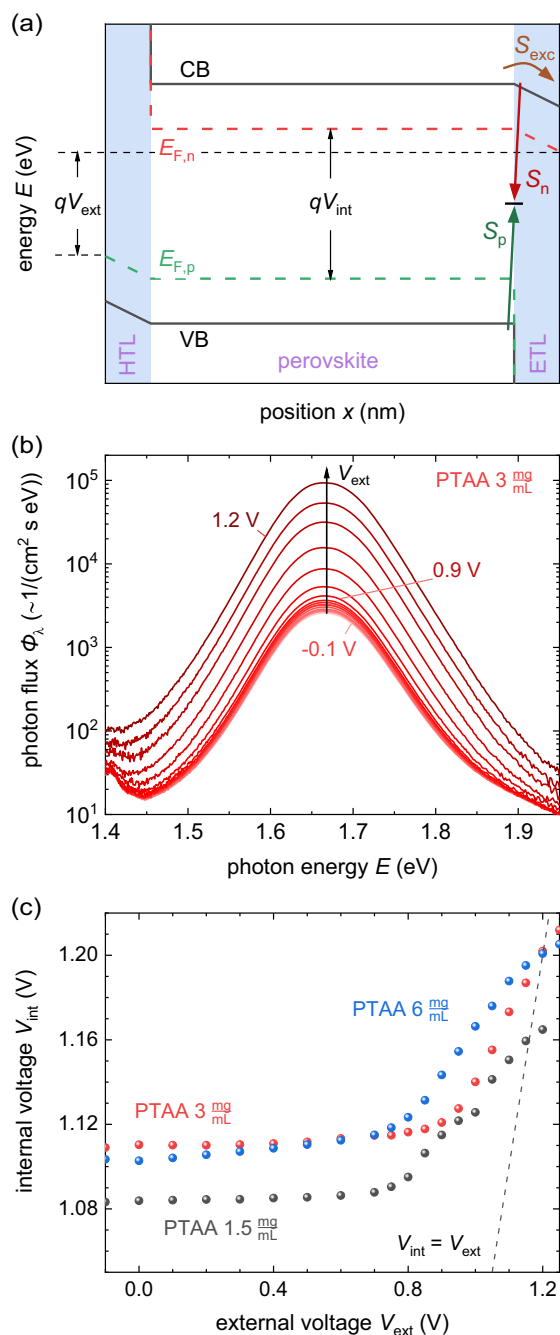
Figure 2. Steady-state PL under operating conditions. a) Band diagram, drawn to illustrate the difference between internal and external voltage. The exchange velocity S_{exc} and the surface recombination velocities S_n and S_p are depicted at the perovskite–ETL interface. The thicknesses and energies are not to scale. b) PL spectra of the PTAA 3 mg mL^{-1} device under varying externally applied bias. The spectra at low voltages are superimposed. c) Connection between the internal and external voltage for the devices with different PTAA thicknesses. The relation $V_{int} = V_{ext}$ is plotted as dashed line for reference.

optical setup as well as physical properties of the sample such as the intrinsic charge carrier concentration or the radiative recombination coefficient. We determine the calibration factor by a

reference measurement of one sample (PTAA 1.5 mg mL^{-1}) at open-circuit conditions where we set the internal voltage equal to the external voltage via $c_{cal} = \phi_{ref,OC} \exp\left(\frac{qV_{ext,ref,OC}}{kT}\right)$. The equality between internal and external voltage is true under open-circuit conditions and if the bands are well aligned in the device.[37] Note that this is not true for other bias conditions as we will see in the following. However, the obtained calibration factor can be used for the calculation of the internal voltage of all other samples and bias conditions. Consider that it is not valid for other perovskites or if the optical setup is changed.

The resulting $V_{int}(V_{ext})$ curve for all devices is plotted in Figure 2c. At open-circuit conditions, we find that $V_{int} = V_{ext}$ is true for all samples, while at lower voltages we find $V_{int} > V_{ext}$. At external voltages $V_{ext} < 0.8$–0.9 V, V_{int} saturates at values around 1.08–1.11 V which means that the discrepancy between V_{int} and V_{ext} increases toward low external voltages. It is noteworthy that, even though the device is at short circuit ($V_{ext} = 0$), there is still a Fermi-level splitting over 1.08 eV inside the perovskite bulk. If we assume for simplicity that the voltage decays only in one CTL, that means there is a billion times higher charge carrier concentration on one side of the CTL (close to the perovskite) in comparison to the other side (close to the electrode).

Given the large differences between internal and external voltages, the classical one-diode model used, for example, for the framework of the Shockley-Queisser model would not be able to describe real solar cells with finite rates of extraction. Based on the rates of recombination and generation, it would be straightforward to formulate a current–voltage curve in terms of the internal voltage as

$$J(V) = qd(R(V) - G) = qd\left[\frac{n_i}{\tau_{eff}(V_{int})}\left(\exp\left(\frac{qV_{int}}{2kT}\right) - 1\right) - G\right]. \tag{6}$$

Here, J is the extracted current density, d the thickness of the perovskite, G the average generation rate throughout the perovskite. In simplified diode models as used in the Shockley–Queisser model, $V_{int} = V_{ext}$ in which case Equation (6) was just the diode equation with the ideality factor of 2.

Describing the current density relative to the internal voltage via Equation (6) does not directly correlate to the measured J–V curve, as it does not contain the external voltage. To obtain a dependence of the current on the external voltage, we look at the drift-diffusion current that arises from the difference of internal and external voltage as previously discussed in refs. [11,28,34,38]. While the internal voltage does not need to be constant inside the bulk, in perovskites this is a good assumption because of the long diffusion length and because the mobile ions will move to create flatband conditions.[29,39–41] Therefore, if the internal and external voltage are found to be different, the voltage drop has to occur over the most resistive layer. This can be easily understood by considering the equation for the current density inside a semiconductor given by

$$J_n(V) = \mu_n n(x)\frac{dE_{F,n}(x)}{dx}, \tag{7}$$

which must hold both in the absorber and in the transport layers. In the transport layers, the product $\mu_n n(x)$ will be lower than in

the perovskite. Thus, the major contribution to the change in $E_{F,n}$ ("voltage drop") will happen in the transport layers (see Figure 2a).[10,11] The current density flowing through, for example, the ETL has to obey Equation (7) and it can be written as a difference between two exponential functions that contain the internal and the external voltage, respectively[34]

$$J_{ETL}(V) = \mu_{ETL} n(x) \frac{dE_{F,n}(x)}{dx}$$
$$= q n_i S_{exc} \left(\exp\left(\frac{qV_{ext}}{2kT}\right) - \exp\left(\frac{qV_{int}}{2kT}\right) \right). \tag{8}$$

Here, S_{exc} is the exchange velocity of the transport layer that describes how quickly charge carriers are exchanged between the electrodes and the perovskite bulk. To avoid confusion, we would like to discuss the difference between the exchange velocity S_{exc} and the more familiar surface recombination velocities S_n and S_p as illustrated on the ETL side of Figure 2a. While both velocities employ the same units, they describe different processes. The surface recombination velocities are usually assumed to be equal for electrons and holes, $S_{rec} = S_n = S_p$, and represent how strongly both carriers interact with trap states that are located at a 2D interface. Minimizing these parameters is critical for optimizing solar cell performance. The exchange velocity indicates how fast the majority carrier (electrons at the ETL side, holes at the HTL side) can be transported through the interface and should be maximized. Here, we stretch the definition from a 2D interface to the whole transport layer. If we assume symmetric transport layers on both sides and constant electric fields in the CTLs, $S_{exc} = \frac{\mu_{CTL} U_{CTL}}{d_{CTL}} \left(1 - e^{-\frac{U_{CTL}}{kT}}\right)^{-1}$ where U_{CTL} is the electrostatic potential difference due to the bending of the bands that shows that S_{exc} is voltage dependent.[10,11] We are able to determine the exact voltage dependence experimentally using Equation (8) because the current density as well as the internal and the external voltage are measured simultaneously in a voltage-dependent PL measurement. Since the current exchanged between absorber and contact as well as the current derived from a generation-recombination balance in the absorber must be equal, we obtain a current–voltage relation that depends on the external voltage via[34,42]

$$J(V) = qd \left(\frac{1}{1 + d/(S_{exc}\tau_{eff})} \right) \left(\frac{n_i}{\tau_{eff}} \left[\exp\left(\frac{qV_{ext}}{2kT}\right) - 1 \right] - G \right). \tag{9}$$

Equation (9) is the classical diode equation with an additional prefactor $\left(1 + \frac{d}{S_{exc}\tau_{eff}}\right)^{-1} \leq 1$, which we identify as a type of collection efficiency[43] and which reduces the extracted current except if $S_{exc}\tau_{eff} \gg d$. The product $S_{exc}\tau_{eff}$ is of unit length and has similar importance as the diffusion or drift length in other solar cell technologies.[44] Only when this typically voltage-dependent extraction length significantly exceeds the absorber thickness d, extraction losses at a given bias condition can be largely avoided. Depending on the behavior of S_{exc} and τ_{eff} with the external voltage, the collection efficiency might decrease the FF as well as the J_{sc} greatly, which shows the difference to an Ohmic series resistance that would mainly affect the FF but just in extreme cases the J_{sc}.[45] The exact effect of the exchange

velocity on the $J–V$ curve and efficiency of these devices will be discussed later in the manuscript. A finite S_{exc} can further explain the apparent photoshunt in the shifted illuminated $J–V$ curve, as well as the ineffectiveness of increasing the diffusion length of the perovskite for device improvements, as discussed before.[11,28] Additionally, S_{exc} can affect either the decay or the rise time in transient photovoltage and current as well as in intensity-modulated photovoltage and -current measurements, depending on its value.[42,46] Another consequence is that the effective recombination decay times vary little over all external voltages for low exchange velocities which we will explain in the following.

4. Relevant Recombination Lifetimes during Steady-State Operation and Comparison to TRPL Decay Times

Figure 3a,b shows the TRPL decays of the three devices as well as the perovskite film on glass in lin–log and log–log scale, respectively. It was possible to measure 2 of the devices (PTAA 1.5 mg mL^{-1} and PTAA 6 mg mL^{-1}) with a dynamic range of 7 orders of magnitude and the PTAA 3 mg mL^{-1} device and the perovskite film with 9 orders of magnitude. All devices behave similarly to each other and, until 200 ns, also to the perovskite film whose decay slows down afterward. It is evident that the PL decays cannot be described by a mono-, bi-, or stretched exponential fit (see Figure S3 and S4, Supporting Information). Nevertheless, we can learn about the carrier dynamics via the concept of the differential decay time τ_{diff}.[25] The idea is to extract a decay time at each point of the curve, so that one can find the behavior of the decay time in relation to the carrier concentration, which can be extracted from the fluence and the PL intensity. From the carrier concentration, we can calculate the internal voltage in the perovskite and from the derivative of the curve we obtain the differential decay time at the corresponding voltage via $\tau_{diff} = -2/\frac{d\ln(\phi)}{dt}$ (half-filled diamonds in Figure 3c). The decay time ranges from small values of 10 ns at high internal voltages to extremely high values up to 50 μs at lower voltages. It does not saturate which indicates that no deep defect dominates the dynamics in the measurable range.[20] All the devices show similar decay times which seemingly contradict the difference in V_{oc} values. The PTAA 1.5 mg mL^{-1} device has a lower V_{oc} than the other two devices and therefore one would expect a shorter recombination lifetime for this device. The contradiction suggests that the obtained decay time does not reflect the recombination lifetime.

Alternatively, one can calculate an effective lifetime from the steady-state data under operating conditions (obtained from voltage-dependent PL) by rearranging Equation (6) and (9), arriving at

$$\tau_{eff} = dq n_0 \frac{\left[\exp\left(\frac{qV_{int}}{2kT}\right) - 1 \right]}{qdG + J} = \frac{qd n_0 \left[\exp\left(\frac{qV_{ext}}{2kT}\right) - 1 \right] - \frac{d}{S_{exc}} J}{qdG + J}. \tag{10}$$

The term $\left(-\frac{d}{S_{exc}} J\right)/(qdG + J)$ takes the difference between V_{int} and V_{ext} into account. Experimentally, the generation rate G is commonly estimated by optical simulations, using the
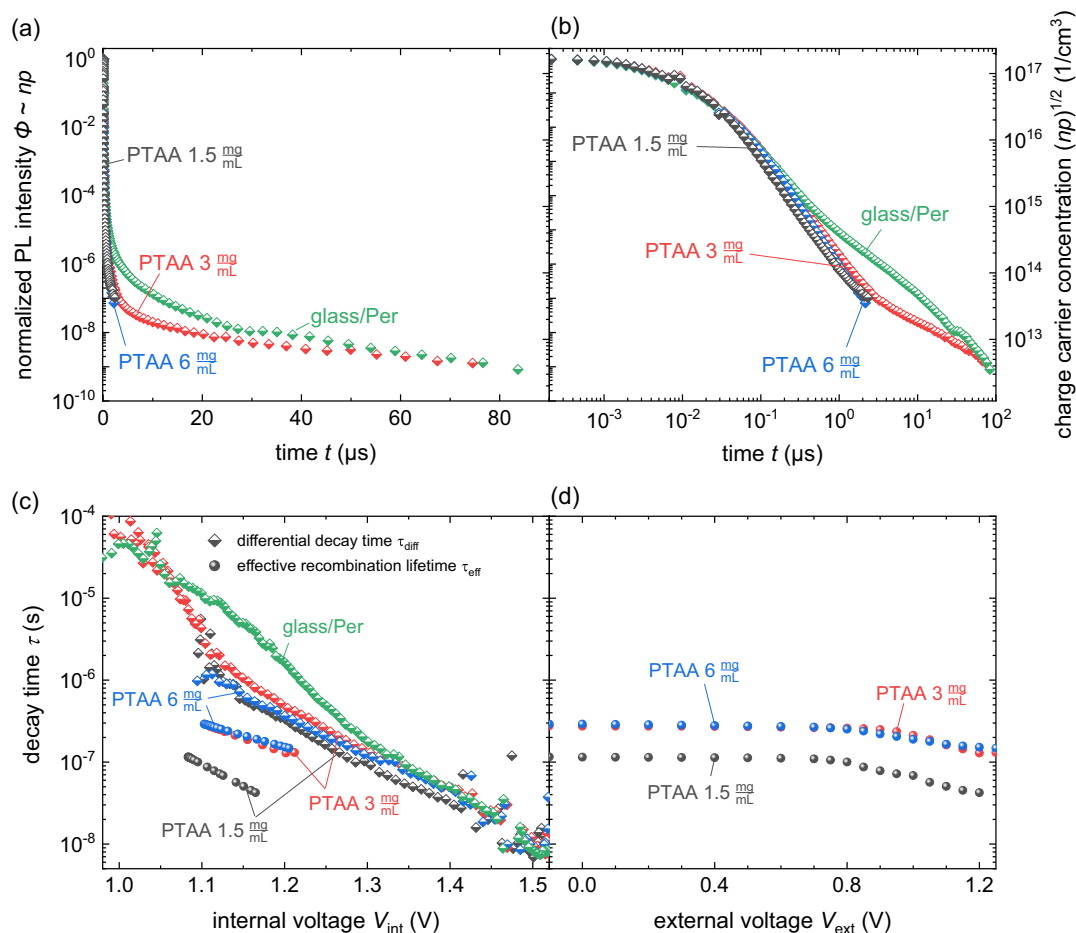
Figure 3. TRPL decay and steady-state recombination decay times. Normalized TRPL decay of the three devices and the perovskite film on glass in a) lin–log and b) log–log scale. The axis on the right shows the corresponding geometric mean of the charge carrier concentration $(np)^{1/2}$ in the perovskite that is related to the PL intensity by $np \approx \phi$. The starting carrier concentration is given by the laser pulse energy density which was $2.3\ \mu J\ cm^{-2}$. Both axes are valid for both panels. c) The extracted differential decay time from the TRPL decay, together with the effective steady-state recombination decay time, extracted from Equation (10), as a function of the internal voltage. d) The effective recombination decay time as a function of the externally applied voltage.

complex refractive index data of the used layers which is often based on many assumptions and gives inaccurate results. Instead, the entire denominator reflects the recombination current density which is calculated via $J_{rec} = qdG + J = J_{sc}\phi^{\frac{1}{n_{id}}}(V_{ext}) / \left(\phi_{oc}^{\frac{1}{n_{id}}} - \phi_{sc}^{\frac{1}{n_{id}}} \right).$[28] That means that with a combined voltage-dependent PL and current measurement and additionally an ideality factor measurement (Figure S5, Supporting Information) we can calculate the effective decay time during steady-state operation. In Figure 3c,d, the results for the discussed solar cells are plotted as a function of the internal and external voltage, respectively. The values range from 40 to 120 ns for PTAA 1.5 mg mL^{-1} and 140 to 290 ns for PTAA 3 and 6 mg mL^{-1}. At the same voltages, the steady-state decay times are lower than the differential decay time of the TRPL measurement. Therefore, it is important to point out possible differences between the two decay times.

The difference can be explained by charging and discharging of the contacts of the solar cells which leads to capacitive effects in the TRPL measurement. Once the charge carriers are created

in the perovskite and an internal voltage is established, they diffuse to the electrodes where the external voltage builds up until the internal and external voltage are equilibrated. The extraction of charge carriers out of the perovskite can be affected by slow transport in the electron and hole transport layers, which we quantify by $S_{exc}.$[42] At open circuit, the electrodes can only discharge by reinjecting electrons and holes into the transport layers and the absorber where they can recombine either in the perovskite or at the perovskite–transport layer interfaces. As a finite exchange velocity also slows this process down, it will lead to longer decay times than the recombination lifetime. In the steady-state measurement, the net current through all layers is constant. Therefore, capacitive effects do not play a role and only recombination should affect the decay time.

However, these capacitive effects cannot fully explain the difference between τ_{eff} and τ_{diff}. We note that the effective recombination decay time τ_{eff} can also be calculated by determining the internal or external voltage at open-circuit conditions under varying light intensities. In this case, $J = 0$ so that G and V_{int}/V_{ext} are the variables in Equation (10). The obtained decay time values

agree well with the voltage-dependent PL method at 1-sun equivalent light intensities and could extend the range of measurable V_{int} (Figure S6a–c, Supporting Information). Importantly, with this method it is also possible to estimate τ_{eff} of films and layer stacks where no external voltage can be applied due to the lack of electrodes. From Figure S6d, Supporting Information, we find that also in the bare perovskite film on glass, the recombination decay times are considerably lower than the differential TRPL decay times at the same internal voltages. In a bare perovskite film at open-circuit conditions, no charges are extracted or injected, so another effect must explain the difference between the decay times. The origin may lay in the photodoping of the perovskite due to defects. Classical doping occurs if the crystal is induced with acceptor-like defects close to the valence band or donor-like defects close to the conductions band. However, even, for example, acceptor-like defects close to the conduction band can lead to an effective doping.[47] It can be imagined that the electron concentration in the conduction band is reduced effectively by fast electron trapping and detrapping in/from the trap state while the hole capture happens much slower. This effect is small in the dark and becomes stronger under illumination and is therefore called photodoping. In a TRPL measurement, photodoping leads to a highly decreased electron concentration in comparison to the hole concentration (or vice versa for a donor-like trap close to the valence band) after long times, so that the change in luminescence is dominated

by the majority carrier. In the steady-state measurement, by assuming the perovskite to be intrinsic, we set $n = p$ and the ideality factor to 2. That means that Equation (10) calculates the decay time of the geometric mean of the electron and hole concentration ($\sqrt{np}$). Therefore, the two measurements determine the decay times of different carrier concentrations, and a comparison is not obvious. This triggers the question of which decay time is relevant for determining, for example, the diffusion length. It might very well be the decay time of the minority carrier which seems to be inaccessible with either method. Answering this question goes beyond the scope of this article and will be discussed in the future.

Even though the light intensity-dependent technique allows for more flexibility in the type of sample, only with voltage-dependent PL we can quantify the recombination decay times that are important at each external voltage point during the steady-state operation of the solar cells (Figure 3d). These are the same values as the spheres in Figure 3c but now plotted as a function of the external voltage. In general, the decay times span a small range with constant decay times from 0 to 0.8 V. This plateau is not the result of a deep trap state as it would be if $\tau_{eff}(V_{int})$ were constant but rather caused by the constant charge carrier density inside the perovskite at different V_{ext}. If charge carrier extraction was more efficient, V_{int} and the recombination rate would be lower and the recombination decay time longer, which would lead to a reduction of the current losses.
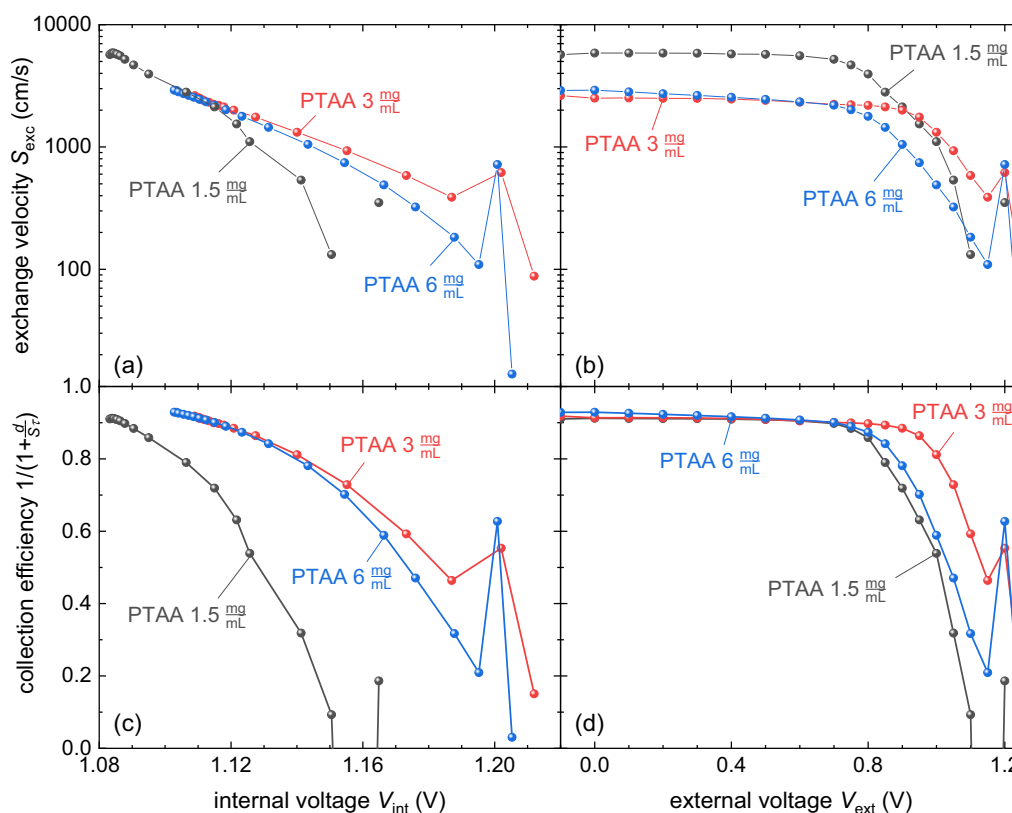

Figure 4. Voltage dependence of the charge carrier extraction. The a,b) exchange velocity and the c,d) collection efficiency as a function of the internal (a,c) and external voltage (b,d). The points around V_{oc} are strongly influenced by measurement uncertainties because they are fractions of very small quantities.

5. Consequences of Slow Charge Exchange on the J–V Curve

Finally, we want to discuss the efficiency losses that the solar cells suffer from the imperfect carrier exchange. To provide an estimate about the magnitude and voltage dependence of S_{exc}, we plotted it as obtained from Equation (8) in **Figure 4**a,b as a function of the internal and external voltage, respectively. S_{exc} ranges from around 6000 cm s^{-1} (PTAA 1.5 mg mL^{-1}) and 3000 cm s^{-1} (PTAA 3 mg mL^{-1} and PTAA 6 mg mL^{-1}) at low voltages to 10–100 cm s^{-1} toward open-circuit conditions where the electric field is minimized. At voltages very close to V_{oc} the experimental determination of S_{exc} is difficult because the current density as well as the term $\left(\exp\left(\frac{qV_{ext}}{2kT}\right) - \exp\left(\frac{qV_{int}}{2kT}\right)\right)$ approach 0 and the fraction of two small quantities is very sensitive to measurement uncertainties. Drift-diffusion simulations indicate that the saturation of S_{exc} at low external voltages is dominated by ions.[28] The ions screen the electric field inside the perovskite, impairing the extraction and limiting S_{exc}.

Figure 4c,d shows the collection efficiency $f_c = \left(1 + \frac{d}{S_{exc}\tau_{eff}}\right)^{-1}$ from Equation (9), that reduces the extracted current when below 1, as a function of the internal and external voltage, respectively. The collection efficiency reaches a maximum of 0.9 at short-circuit conditions and in the plateau until $V_{ext} = 0.8$ V and goes toward 0 for open-circuit conditions. Especially, the constant nonunity collection efficiency at low external voltages is important to notice because often it is assumed that at short circuit all generated charge carriers are extracted, whereas we show here that the J_{sc} can suffer from high extraction losses of 10%. The collection efficiency at short-circuit conditions can be simplified to $f_c(0V) = 1 - \left(\frac{\phi_{sc}}{\phi_{oc}}\right)^{\frac{1}{n_{id}}}$ which can give a fast estimate of the quality of extraction in the measured device (Figure S7, Supporting Information).[34] The value of f_c at short-circuit conditions is similar for all the PTAA concentrations which indicates that the trend of the J_{sc} in Figure 1c is of optical origin as supported by the absorbance data in Figure S8, Supporting Information. Toward higher voltages, S_{exc} decreases due to the reduced electric field inside the transport layers and τ_{eff} decreases due to the increase charge carrier concentration in the perovskite. Both effects lead to a reduction in the collection efficiency. At maximum power point, f_c should ideally be unity, but it falls to around 70–80%. Even though both devices exhibit a similar V_{oc}, the collection efficiency of the PTAA 6 mg mL^{-1} device is less than the one of the PTAA 3 mg mL^{-1} device at the same voltages which explains the lower FF.

With the knowledge about the collection efficiency $\left(1 + \frac{d}{S_{exc}(V_{ext})\tau_{eff}(V_{ext})}\right)^{-1}$ from Figure 4d, we can find the limit of the J–V curve when the exchange is infinitely fast ($S_{exc} \to \infty$). To do so, we divide the current density by the corresponding collection efficiency f_c at each external voltage point of the J–V_{ext} curve, obtained during the voltage-dependent PL measurement. The calculated limits of the J–V curves and the extracted power densities from the example of the device PTAA 3 mg mL^{-1} are plotted in **Figure 5**a,b, respectively (the corresponding figures for the other devices can be found in Figure S9 and S10, Supporting Information). The J_{sc} of the limit is
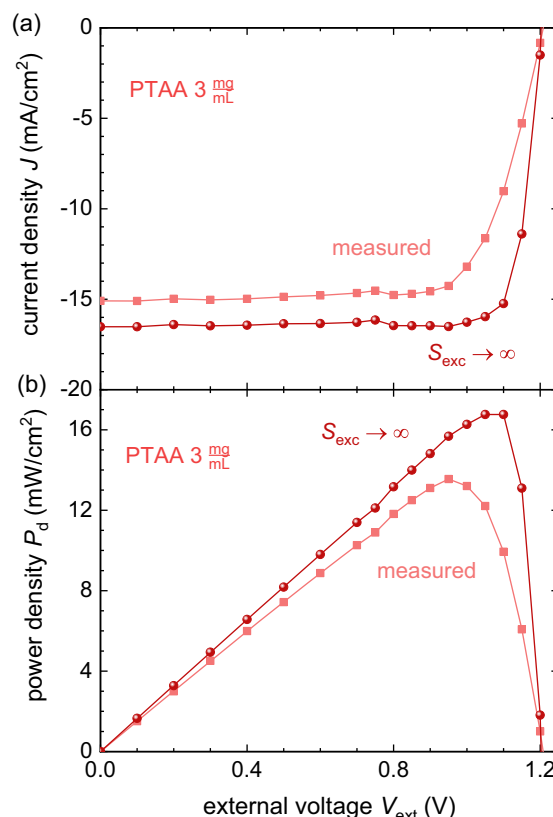
Figure 5. Performance potential when the exchange is perfect. a) J–V curve of the device PTAA 3 mg mL^{-1} as measured during the voltage-dependent PL measurement and the potential curve for perfect exchange conditions. b) The calculated power density curves for the same cases.

increased by the inverse of the collection efficiency leading to a considerable improvement. Furthermore, the FF is increased by shifting the maximum power point to a higher external voltage. These two enhancements would result in a 3% absolute improvement potential in PCE for these solar cells that could be realized if there was perfect charge carrier extraction. The results highlight the importance of improving the mobility of the CTLs to not just increase the FF but also J_{sc}.

6. Conclusion

We quantify the exchange velocity S_{exc} by voltage-dependent photoluminescence measurements and thereby determine the losses in current and power density due to extraction problems in perovskite solar cells. With the additional knowledge of the ideality factor, we can calculate the effective steady-state recombination decay time of the charge carriers as a function of the internal as well as external voltage. Applied to wide-bandgap coevaporated perovskite solar cells, this procedure shows recombination decay times in the order of 40–300 ns which is significantly lower than the TRPL decay times at the same carrier concentration showing that capacitive effects prolong the latter. Furthermore, we found that the voltage-dependent exchange velocity leads to short-circuit current losses of about 10% and FF losses of 8%. The developed

technique allows for the classification of experimental decay times in terms of recombination and for an estimation of transport losses during the steady-state operation of the solar cell opening the door for improvements of the CTLs for better charge extraction.

7. Experimental Section

Materials: All materials were used as received without further purification. Methylammonium iodide (MAI, >99.0%), lead(II) iodide (PbI_2, 99.999%, trace metals basis), lead(II) bromide ($PbBr_2$, 99.99%), PTAA, and bathocuproine (BCP) were purchased from Luminescence Technology Corp. Fullerene C_{60} (>99.95%) was purchased from Creaphys.

Perovskite Thin Films and Solar Cells Fabrication: (ITO-coated) glass substrates were subsequently cleaned in soap, water, and isopropanol, followed by O_2 plasma treatment. PTAA was spin coated inside a glove box from a toluene solution with three different concentrations (1.5, 3, and 6 mg mL^{-1}). The thicknesses of the PTAA layers were measured with an Ambios XP-1 profilometer and averaged to 10, 32, and 45 nm, respectively. The films were annealed at 100 °C for 10 min afterward. Substrates were transferred to a vacuum chamber integrated into a nitrogen-filled glovebox and evacuated to a pressure of 10^{-6} mbar for the vapor-phase deposition. One vacuum chamber was used to sublime C_{60} and BCP, while the perovskite was deposited in a second chamber. All sources had a dedicated quartz crystal microbalance (QCM) sensor above, and an additional one was installed close to the substrates for the overall deposition rate measurement. All sources were individually calibrated for their respective materials and no cross-reading between the different QCMs was ensured by the relative position of the sources, shutters, and sensors. Typical sublimation temperatures for the precursors were ≈125 °C for MAI and 310 °C for $Pb(I_{1-x}Br_x)_3$. The mixed halide precursor $Pb(I_{1-x}Br_x)_3$ was prepared by mixing in an alumina crucible the calculated amounts of PbI_2 and $PbBr_2$, and by heating them at 350 °C for 5 min after complete melting of the mixture. The deposition rate for C_{60} was 0.5 Å s^{-1} while the thinner BCP layer was sublimed at 0.2 Å s^{-1}. Ag was deposited in a third vacuum chamber from alumina-coated aluminum boats and by applying currents ranging from 2.0 to 4.5 A.

Atomic Layer Deposition Encapsulation: An Arradiance's GEMStar XT Thermal atomic layer deposition (ALD) system integrated into a nitrogen-filled glovebox was used. The ALD chamber was heated to 40 °C, while the precursor and oxidizer manifolds (to which the bottles of trimethylaluminum, TMA, and water were connected) were heated to 115 and 140 °C, respectively, to avoid vapor accumulation at the tubes leading to the main chamber. Prior to deposition, the tubes and valves were degassed three times by performing pulses with the bottles manually closed, to avoid contamination. The edges of the ITO and AG contacts of the devices were protected with Dupont's polyimide Kapton tape and the substrates were inserted in the chamber, which was then evacuated. A N_2 gas flow of 20 SCCP was used as TMA and water vapor carrier. A cycle consisted of consecutive purges of TMA for 10 ms and water vapor for 30 ms, each followed by N_2 purges for enough time to guarantee complete removal of the precursors from the ALD chamber, as monitored by the transient pressure inside the chamber. The process consisted of 300 consecutive cycles, resulting in a 30 nm-thick alumina layer.

Characterization: Absorption spectra were collected using fiber optics-based Avantes Avaspec2048 Spectrometer. The crystalline structure of the thin films was studied by XRD. The patterns were collected in Bragg–Brentano geometry on an Empyrean PANalytical powder diffractometer with a copper anode operated at 45 kV and 40 mA.

The current–voltage curves were measured by a calibrated AM1.5 spectrum of a class AAA solar simulator (WACOM-WXS-140S-Super-L2 with a combined xenon/ halogen lamp-based system) providing a power density of 100 mW cm^{-2}. A 2450 Keithley was used as a source measure unit. All measurements were carried out under inert atmosphere in glovebox.

For the steady-state photoluminescence measurement, all samples were optically excited by a continuous wave 532 nm laser (Coherent Sapphire) through the glass substrate. The laser power was 17.3 mW and the beam was widened to a square of about 5.3 × 5.3 mm to illuminate the entire cell area (4 × 4 mm). The luminescence spectra were detected via a spectrometer (Andor Shamrock 303) with an Andor Si (deep depletion) charge-coupled device (CCD) camera (iDus Series). The detection path was calibrated to relative intensity using a halogen lamp with known spectrum. During the measurements, dark spectra were taken followed each illuminated measurement to subtract the background. The samples were kept in an airtight holder under inert atmosphere. For the voltage-dependent PL measurements, the solar cells were contacted to a 2450 Keithley source measure unit and the laser power was reduced with a 0.3 OD neutral density filter to match the current density under AM1.5G conditions which corresponded to a laser power density of about 61 mW cm^{-2}. To determine the ideality factor and for the intensity dependence, PL measurements were performed with different laser intensities ϕ_{laser} impinging on the sample by using different neutral density (ND) filters. The internal voltage of the samples was calculated using the simultaneous measurement of V_{ext} and PL of one well-performing solar cell at open-circuit conditions as a reference by defining a calibration factor $c_{cal} = \exp\left(\frac{V_{ext,ref,OC}}{kT}\right) \times \int \phi^\lambda_{ref,oc} d\lambda$ where we integrated the PL spectrum ϕ^λ over all wavelengths λ where the PL peak lay. The internal voltage of all other measurements (different samples, light intensities, external voltages) was obtained by integrating the spectra and applying the calibration factor via $V_{int} = \frac{kT}{q} \ln\left(\frac{\int \phi^\lambda d\lambda}{c_{ref}}\right)$. Once $V_{int}(V_{ext})$ or $V_{int}(\phi_{laser})$ were established, the effective decay time can be calculated by Equation (10) and the definition of the recombination current as explained in the main text. For the glass/per sample, the recombination current cannot be calculated because the J_{sc} was not known. Therefore, we used the recombination current at open circuit from the $V_{int}(V_{oc})$ measurement of the PTAA 1.5 mg mL^{-1} sample to calculate the generation rate G_{1sun} at 1 sun equivalence and scaled G according to the laser ND filter used. In total, the decay time for the light intensity-dependent measurements was calculated via $\tau_{eff} = n_0 \left(\exp\left(\frac{qV_{int}}{2kT}\right) - 1\right) \left(10^{-(OD-0.3)} G_{1sun}\right)^{-1}$, where OD corresponds to the optical density of the neutral density filter. By equating the generation rate in the glass/per and the PTAA 1.5 mg mL^{-1} sample, we introduced a small uncertainty. However, at open-circuit conditions a potential error in G was less sensitive and negligible.

For TRPL measurements, all samples were excited through the glass substrate with a pulsed UV-solid-state laser (100 Hz), which served as a pump laser for a dye laser. The pumped dye (Coumarin) emitted down-converted, pulsed laser radiation of 513 nm. This radiation passed through an optical fiber and impinged at an angle of 30° on the sample surface and illuminated an elliptical shaped spot with a diameter of 3.1 mm. The emitted photoluminescence was focused and coupled into a spectrometer (sPEX 270M from Horiba Jobin Yvon). Edge filters placed in front of the entrance slit of the spectrometer suppressed scattered light from the laser. In the spectrometer, the PL beam was diffracted by the grating unit (150 lines mm^{-1}, 500 nm blaze) and spectrally dispersed. The spectrally dispersed signal was then detected with a gated CCD camera (iStar DH320T-18U-73 from Andor Solis), where the signal was first converted into an electrical signal by a (Multi Alkali) photocathode and amplified by a microchannel plate (MCP), to be then back converted using a phosphor (P43) screen, and finally detected with a CCD chip consisting of an array of 1024 × 256 pixels. In order to perform time-resolved measurements, the inherent shutter-gate functionality of the camera was exploited by reverse poling of the voltages between photocathode and MCP. Gating times were triggered by a partial signal of the laser pulse in combination with applying different delay times between the trigger signal and the actual opening of the gate. In this way, one can get a PL spectrum for different delay times after the laser pulse. In addition, the applied voltage across the microchannel plate controlled the acceleration of the photoelectrons and by this their multiplication and the resulting amplification of the PL signal. This gain, in combination with the shutter-gate width, integration time, binning of the pixels, and number of accumulations, can be adjusted to maximize the intensity of the signal to use

the capabilities of the detector in an optimal way. To increase the dynamic range of this method and to get the decay time values for a wide range of V_{int}, we developed a routine, where several measurements starting at different delay times after the laser-pulse excitation were stitched together. Conducting additional measurements at later delay times allowed us to adjust the measurement parameters like the MPC gain or the camera-integration time, which went along with a higher signal-to noise ratio. The first measurement, starting just before the laser pulse, was quite fast and usually took only several minutes. Here, the width of the gate pulse was set for the first measurement to the minimum (2 ns). The measurements at higher delay times between the trigger signal and the actual opening of the gate required a higher integration time to get a good signal which can be shortened by increasing the gate width (to around a fifth of the measured decay time at this delay time), the gain, or the binning of the pixels. The applied energy density was $\approx$2300 nJ cm^{-2}. To get the TRPL decay, the background-subtracted PL spectrum at each delay time was integrated over the energy region where the PL peaks were. Finally, the TRPL signal was normalized.

In order to plot the decay time as a function of the internal voltage V_{int}, we needed to determine V_{int}. The maximum value of the internal voltage $V_{int,max}$ directly at the end of the laser pulse was calculated by measuring the absorbed laser fluence. From the fluence and the absorber thickness d, the absorbed photon density and from there the average charge carrier density per volume laser n were calculated. Now we assumed that the sample was in high-level injection at early times ($n = p$) and calculated the Fermi-level splitting from Equation (5) of the main text where $n_i = 1.7 \times 10^4$ cm^{-3} is the intrinsic charge carrier density in the MAPb(I$_{0.85}$Br$_{0.15}$)$_3$ perovskite. Then we used the fact that there is always an exponential relation between the quasi-Fermi-level splitting and the photoluminescence flux ϕ, which would allow us to write $\phi \propto \exp\left(\frac{qV_{int}}{kT}\right)$. This proportionality implies that any order of magnitude decrease of the TRPL decay corresponds to a relative change in quasi-Fermi-level splitting of $\approx$60 meV. Alternatively, one could omit the absolute calibration of the x-axis and plot the decay time as a function of $\ln(\phi)$, leading to the same shape of the decay time curve.

Supporting Information

Supporting Information is available from the Wiley Online Library or from the author.

Acknowledgements

Conflict of Interest

The authors declare no conflict of interest.

Author Contributions

Chris Dreessen: Conceptualization (supporting); Data curation (lead); Formal analysis (lead); Funding acquisition (supporting); Investigation (lead); Methodology (lead); Project administration (lead); Software (lead); Validation (lead); Visualization (lead); Writing—original draft (lead); Writing—review & editing (equal). **Lidón Gil-Escrig**: Investigation (supporting); Methodology (supporting); Writing—review & editing (supporting). **Markus Hülsbeck**: Methodology (supporting); Software (supporting); Validation (supporting). **Michele Sessolo**: Funding acquisition (supporting); Project administration (equal); Writing—review & editing (supporting). **Henk J. Bolink**: Funding acquisition (equal); Project administration (equal); Resources (equal); Supervision (equal); Writing—review & editing (supporting). **Thomas Kirchartz**: Conceptualization (lead); Funding acquisition (equal); Project administration (equal); Resources (equal); Software (equal); Supervision (lead); Validation (supporting); Visualization (supporting); Writing—review & editing (equal).

Data Availability Statement

The data that support the findings of this study are available from the corresponding author upon reasonable request.

Keywords

[1] Best Research-Cell Efficiency Chart | Photovoltaic Research | NREL, https://www.nrel.gov/pv/cell-efficiency.html (accessed: October 2024)

[2] J. H. Noh, S. H. Im, J. H. Heo, T. N. Mandal, S. Il Seok, *Nano Lett.* **2013**, *13*, 1764.

[3] M. Jošt, L. Kegelmann, L. Korte, S. Albrecht, *Adv. Energy Mater.* **2020**, *10*, 1904102.

[4] S. de Wolf, J. Holovsky, S. J. Moon, P. Löper, B. Niesen, M. Ledinsky, F. J. Haug, J. H. Yum, C. Ballif, *J. Phys. Chem. Lett.* **2014**, *5*, 1035.

[5] A. Miyata, A. Mitioglu, P. Plochocka, O. Portugall, J. T. W. Wang, S. D. Stranks, H. J. Snaith, R. J. Nicholas, *Nat. Phys.* **2015**, *11*, 582.

[6] E. Gutierrez-Partida, H. Hempel, S. Caicedo-Dávila, M. Raoufi, F. Peña-Camargo, M. Grischek, R. Gunder, J. Diekmann, P. Caprioglio, K. O. Brinkmann, H. Köbler, S. Albrecht, T. Riedl, A. Abate, D. Abou-Ras, T. Unold, D. Neher, M. Stolterfoht, *ACS Energy Lett.* **2021**, *6*, 1045.

[7] J. M. Richter, M. Abdi-Jalebi, A. Sadhanala, M. Tabachnyk, J. P. H. Rivett, L. M. Pazos-Outón, K. C. Gödel, M. Price, F. Deschler, R. H. Friend, *Nat. Commun.* **2016**, *7*, 13941.

[8] D. W. Dequilettes, S. Koch, S. Burke, R. K. Paranji, A. J. Shropshire, M. E. Ziffer, D. S. Ginger, *ACS Energy Lett.* **2016**, *1*, 438.

[9] I. L. Braly, D. W. Dequilettes, L. M. Pazos-Outón, S. Burke, M. E. Ziffer, D. S. Ginger, H. W. Hillhouse, *Nat. Photonics* **2018**, *12*, 355.

[10] O. J. Sandberg, J. Kurpiers, M. Stolterfoht, D. Neher, P. Meredith, S. Shoaee, A. Armin, *Adv. Mater. Interfaces* **2020**, *7*, 2000041.

[11] S. Akel, A. Kulkarni, U. Rau, T. Kirchartz, *PRX Energy* **2023**, *2*, 013004.

[12] T. Kirchartz, J. A. Márquez, M. Stolterfoht, T. Unold, *Adv. Energy Mater.* **2020**, *10*, 1904134.

[13] S. Rein, *Lifetime Spectroscopy*, Springer Berlin Heidelberg, Berlin, Heidelberg **2005**.

[14] F. Peña-Camargo, J. Thiesbrummel, H. Hempel, A. Musiienko, V. M. Le Corre, J. Diekmann, J. Warby, T. Unold, F. Lang, D. Neher, M. Stolterfoht, *Appl. Phys. Rev.* **2022**, *9*, 021409.

[15] I. Levine, S. Gupta, A. Bera, G. Ceratti, G. Hodes, D. Cahen, D. Guo, T. J. Savenije, J. Ávila, H. J. Bolink, O. Millo, D. Azulay, I. Balberg, *J. Appl. Phys.* **2018**, *124*, 103103.

[16] L. Krückemeier, Z. Liu, B. Krogmeier, U. Rau, T. Kirchartz, *Adv. Energy Mater.* **2021**, *11*, 2102290.

[17] D. Kiermasch, A. Baumann, M. Fischer, K. Tvingstedt, *Energy Environ. Sci.* **2018**, *11*, 629.

[18] C. M. Wolff, S. A. Bourelle, L. Q. Phuong, J. Kurpiers, S. Feldmann, P. Caprioglio, J. A. Marquez, J. Wolansky, T. Unold, M. Stolterfoht, S. Shoaee, F. Deschler, D. Neher, *Adv. Energy Mater.* **2021**, *11*, 2101823.

[19] J. Bisquert, *J. Phys. Chem. Lett.* **2022**, *13*, 7320.

[20] Y. Yuan, G. Yan, C. Dreessen, T. Rudolph, M. Hülsbeck, B. Klingebiel, J. Ye, U. Rau, T. Kirchartz, *Nat. Mater.* **2024**, *23*, 391.

[21] L. Gil-Escrig, I. Susic, İ. Doğan, V. Zardetto, M. Najafi, D. Zhang, S. Veenstra, S. Sedani, B. Arikan, S. Yerci, H. J. Bolink, M. Sessolo, *Adv. Funct. Mater.* **2023**, *33*, 2214357.

[22] M. Taddei, S. Jariwala, R. J. E. Westbrook, S. Gallagher, A. C. Weaver, J. Pothoof, M. E. Ziffer, H. J. Snaith, D. S. Ginger, *ACS Energy Lett.* **2024**, *9*, 2508.

[23] J. Tong, J. Tong, Z. Song, D. H. Kim, X. Chen, C. Chen, A. F. Palmstrom, P. F. Ndione, M. O. Reese, S. P. Dunfield, O. G. Reid, J. Liu, F. Zhang, S. P. Harvey, Z. Li, S. T. Christensen, G. Teeter, D. Zhao, M. M. Al-jassim, M. F. A. M. Van Hest, M. C. Beard, S. E. Shaheen, J. J. Berry, Y. Yan, K. Zhu, *Science* **2019**, *364*, 475.

[24] B. Krogmeier, F. Staub, D. Grabowski, T. Kirchartz, U. Rau, *Sustainable Energy Fuels* **2018**, *2*, 1027.

[25] L. Krückemeier, B. Krogmeier, Z. Liu, U. Rau, T. Kirchartz, *Adv. Energy Mater.* **2021**, *11*, 2003489.

[26] W. Shockley, W. T. Read, *Phys. Rev.* **1952**, *87*, 835.

[27] J. Euvrard, Y. Yan, D. B. Mitzi, *Nat. Rev. Mater.* **2021**, *6*, 531.

[28] D. Grabowski, Z. Liu, G. Schöpe, U. Rau, T. Kirchartz, *Sol. RRL* **2022**, *6*, 2200507.

[29] B. Das, Z. Liu, I. Aguilera, U. Rau, T. Kirchartz, *Mater. Adv.* **2021**, *2*, 3655.

[30] P. Caprioglio, M. Stolterfoht, C. M. Wolff, T. Unold, B. Rech, S. Albrecht, D. Neher, *Adv. Energy Mater.* **2019**, *9*, 1901631.

[31] N. Wu, Y. Wu, D. Walter, H. Shen, T. Duong, D. Grant, C. Barugkin, X. Fu, J. Peng, T. White, K. Catchpole, K. Weber, *Energy Technol.* **2017**, *5*, 1827.

[32] M. Stolterfoht, V. M. le Corre, M. Feuerstein, P. Caprioglio, L. J. A. Koster, D. Neher, *ACS Energy Lett.* **2019**, *4*, 2887.

[33] C. Dreessen, D. Pérez-del-Rey, P. P. Boix, H. J. Bolink, *J. Lumin.* **2020**, *222*, 117106.

[34] U. Rau, V. Huhn, B. E. Pieters, *Phys. Rev. Appl.* **2020**, *14*, 014046.

[35] D. Hinken, K. Bothe, K. Ramspeck, S. Herlufsen, R. Brendel, *J. Appl. Phys.* **2009**, *105*, 104516.

[36] M. Pranav, A. Shukla, D. Moser, J. Rumeney, W. Liu, R. Wang, B. Sun, S. Smeets, N. Tokmoldin, Y. Cao, G. He, T. Beitz, F. Jaiser, T. Hultzsch, S. Shoaee, W. Maes, L. Lüer, C. Brabec, K. Vandewal, D. Andrienko, S. Ludwigs, D. Neher, *Energy Environ. Sci.* **2024**, *17*, 6676.

[37] M. Stolterfoht, P. Caprioglio, C. M. Wolff, J. A. Márquez, J. Nordmann, S. Zhang, D. Rothhardt, U. Hörmann, Y. Amir, A. Redinger, L. Kegelmann, F. Zu, S. Albrecht, N. Koch, T. Kirchartz, M. Saliba, T. Unold, D. Neher, *Energy Environ. Sci.* **2019**, *12*, 2778.

[38] O. Breitenstein, *IEEE J. Photovoltaics* **2014**, *4*, 899.

[39] S. D. Stranks, G. E. Eperon, G. Grancini, C. Menelaou, M. J. P. Alcocer, T. Leijtens, L. M. Herz, A. Petrozza, H. J. Snaith, *Science* **2013**, *342*, 341.

[40] N. Tessler, Y. Vaynzof, *ACS Energy Lett.* **2020**, *5*, 1260.

[41] P. Calado, A. M. Telford, D. Bryant, X. Li, J. Nelson, B. C. O'Regan, P. R. F. Barnes, *Nat. Commun.* **2016**, *7*, 13831.

[42] L. Krückemeier, Z. Liu, T. Kirchartz, U. Rau, *Adv. Mater.* **2023**, *35*, 2300872.

[43] R. S. Crandall, *J. Appl. Phys.* **1998**, *54*, 7176.

[44] T. Kirchartz, J. Bisquert, I. Mora-Sero, G. Garcia-Belmonte, *Phys. Chem. Chem. Phys.* **2015**, *17*, 4007.

[45] M. A. Green, *Solar Cells: Operating Principles, Technology and System Applications Paperback*, Prentice Hall, Englewood Clirrs, NJ **1982**.

[46] S. Ravishankar, L. Kruppa, S. Jenatsch, G. Yan, Y. Wang, *Energy Environ. Sci.* **2024**, *17*, 1229.

[47] B. Das, I. Aguilera, U. Rau, T. Kirchartz, *Adv. Opt. Mater.* **2022**, *10*, 2101947.